Low-Power, Bio-Inspired Time-Stamp-Based 2-D Optic Flow Sensor for Artificial Compound Eyes of Micro Air Vehicles

Seokjun Park, Kyuseok Lee, Hyunsoo Song, *Student Member, IEEE*, Jihyun Cho, Sung-Yun Park, *Member, IEEE*, and Euisik Yoon, *Member, IEEE*

***Abstract*— We report a low-power, bio-inspired mixed-signal 2-D optic flow sensor to realize artificial compound eyes, which can provide a wide field of view (FoV) sensing capability for autonomous navigation of micro-air-vehicles (MAVs). Inspired by insect vision, a 2-D time-stamp algorithm has been developed to scale the number of deployable sensors at low power. The fabricated sensor estimates 16-b 2-D optic flows of maximum 1.96 rad/s with FoV of 60° from the integrated mixed-signal algorithm core, which consumes only 243.3 pJ/pixel or ∼30 μW at 120 fps. In addition, the peripheral circuits for modular design have been integrated on chip to provide optic flow data compression, wide-field integration (WFI), and serial peripheral interface (SPI). More than 25 sensors can be connected in a single SPI bus and transmit the full resolution optic flows. The fabricated prototype sensor supports full resolution 2-D optic flows from an array of 64 x 64 pixels at 120 fps through a 3 MB/s SPI bus (4 wires total).**

***Index Terms*— Artificial compound eyes, autonomous navigation, 2-D optic flow, micro-air-vehicle (MAV), wide-field integration (WFI).**

I. Introduction

RECENTLY, miniaturized artificial compound eyes have been recognized as a promising approach to provide wide-field visual information for micro-air-vehicle (MAV) applications [1]–[4]. The extremely small size and payload constraints of the MAVs, in the order of tens of millimeters and grams, have inspired robot researchers to discover new navigation mechanisms inside flying insect since the conventional solutions cannot satisfy the challenging design constraints [5]. Flying insects, despite their small size, have the impressive ability to navigate their surroundings by utilizing the optic flow from their wide field-of-view (FoV) vision through miniaturized compound eyes. By integrating wide-field optic flow and applying the matched filters, the flying insects can effectively extract key clues for estimating their flying status. For example, the distance from possible obstacles, the speed of flight, and the self-motion of a vehicle can be decoded from the wide-field integration (WFI) of the optic flow. Based on this WFI-based navigation scheme, a few unmanned bio-inspired robots have been successfully reported. A 10-gram flying robot mounting two miniaturized 1-D optic flow sensing systems as their left and right eyes, demonstrated their bio-inspired collision avoidance control scheme by steering the body to the opposite direction from the region that gives dense and large optic flows, which is the strong indication that the vehicle is approaching close to an object [6], [7]. Another types of bio-inspired robots that extract control parameters from WFIs are also demonstrated [8]–[10]. Research efforts have also been made to realize bio-inspired artificial compound eyes by mimicking the wide FoV of insect visual organs [2], [4]. However, complicated fabrication processes were required to implement a hemispherical lens configuration and secure an independent optical path in each photoreceptor. Also, the micro lens design is challenging in order to precisely mimic the compound eyes geometry for an accurate control of the acceptance and inter-photoreceptor angles.

In this work, we propose an integrated low-power 2-D optic flow sensor that can be configured in a semi-hemispherical platform, mimicking miniaturized compound eyes in a small form factor. The platform can be easily fabricated by using a flexible PCB, therefore it does not require any complicated fabrication procedures and specially-designed micro lens. Fig. 1 shows the diagram of our conceptual artificial compound eyes. The flexible semi-hemispherical platform is designed to provide the wide-field optic flow sensing, which covers 180° FoV like a compound eye in flying insects. To realize the wide FoV, the system has multiple optic flow sensors mounted on a flat flexible PCB, followed by shaping the PCB module to form a desired inter-sensor angle as in an origami.

Manuscript received July 26, 2019; accepted August 18, 2019. Date of publication August 30, 2019; date of current version November 26, 2019. This work was supported in part by the U.S. Army Research Laboratory under Contract W911NF and in part by the Microelectronics Center of Micro Autonomous Systems and Technology (MAST) Collaborative Technology Alliance (CTA). The associate editor coordinating the review of this article and approving it for publication was Dr. Cheng-Ta Chiang. *(Corresponding authors: Sung-Yun Park; Euisik Yoon.)*

S. Park, K. Lee, and H. Song are with the Center for Wireless Integrated MicroSensing and Systems, University of Michigan, Ann Arbor, MI 48109 USA, and also with the Department of Electrical Engineering and Computer Science, University of Michigan, Ann Arbor, MI 48109 USA (e-mail: joon0101@gmail.com; eekslee@umich.edu; hyunsoos@umich.edu).

J. Cho is with Apple Inc., Cupertino, CA 95014 USA (e-mail: jihyun_cho@apple.com).

S.-Y. Park is with the Center for Wireless Integrated MicroSensing and Systems, University of Michigan, Ann Arbor, MI 48109 USA, also with the Department of Electrical Engineering and Computer Science, University of Michigan, Ann Arbor, MI 48109 USA, and also with the Department of Electronics Engineering, Pusan National University, Busan 46241, Korea (e-mail: sungyun@pusan.ac.kr).

E. Yoon is with the Center for Wireless Integrated MicroSensing and Systems, University of Michigan, Ann Arbor, MI 48109 USA, also with the Department of Electrical Engineering and Computer Science, University of Michigan, Ann Arbor, MI 48109 USA, also with the Center for Nanomedicine, Institute for Basic Science (IBS), Yonsei University, Seoul 03722, Korea, also with the Graduate Program of Nano Biomedical Engineering, Yonsei-IBS Institute, Yonsei University, Seoul 03722, Korea (e-mail: esyoon@umich.edu).

Digital Object Identifier 10.1109/JSEN.2019.2938559

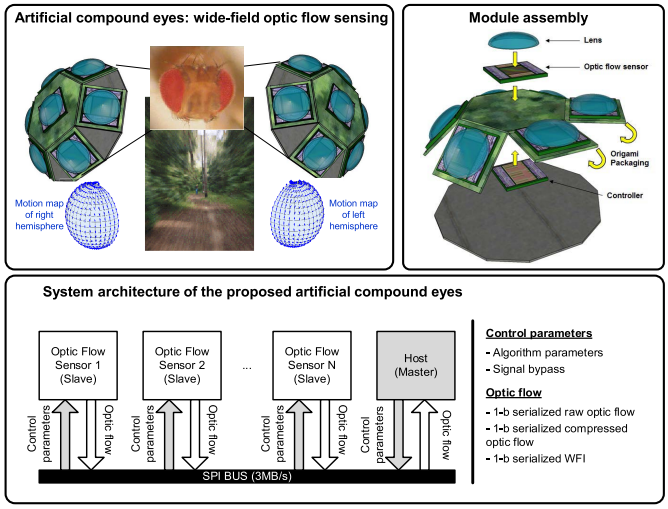

Fig. 1. The conceptual diagram of the proposed artificial compound eye optic flow sensing platform.

For the proposed artificial compound eye being practically realizable, each sensor must provide the low-power operation. But most previous works mainly focused on an insect's motion estimation in digital VLSI circuit implementations, resulting in large power consumption [9], [11]–[15]. Conventional optic flow algorithms, such as Lucas and Kanade, have huge amount of numerical calculation loads; therefore they require digital hardware with high computing power (CPU and/or FPGA). As an alternative approach for low-power optic flow sensor implementation, the bio-inspired neuromorphic algorithms have been realized in analog circuits [16]–[20] or combination of analog and digital circuits [21]–[24]. However, pure analog signal processing is susceptible to temperature and process variations and it must be implemented in pixel-level circuits; as a result, it is extremely difficult to scale the pixel size [20]. The combination of the analog and digital circuits has provided compromised solutions but the power consumption is still in the range of a few hundreds of mW due to the lack of the resource optimization between the customized analog pixels and the off-the-shelf digital processing components [23]. More recently, various neuromorphic vision sensors were further developed based on logarithmic photoreceptors [25], including asynchronous time-based image sensor (ATIS) [26], dynamic vision sensor (DVS) [27], and dynamic and active-pixel vision sensor (DAVIS) [28]. These are event-based CMOS imagers where the pixels immediately respond to the contrast change of the scene. They have demonstrated low latencies (a few μs) and high dynamic ranges exceeding 120 dB for visual navigation, but are not compatible with the conventional frame-based vision algorithms due to their asynchronous response. Event-based optic flow sensors were reported for control of MAVs [29], [30]. However, pixel fill factors are relatively low ($<$10%) and overall power consumption is over a few tens of mW, which make them not suitable for being deployed in artificial compound eye modules.

To implement a low-power bio-inspired optic flow sensor, we first have devised a time-stamp-based optic flow algorithm in analog and mixed-signal domain, which is modified from the conventional elementary motion detector (EMD) algorithm found in insect eyes [22]–[24]. In implementing this algorithm, we optimized the partitioning of hardware blocks in analog and digital domains as well as allocation of functional blocks in pixel-level, column- level, and chip-level processing units [31], [32]. Temporal filtering, which requires huge hardware resources if implemented in the digital domain, moved into a pixel-level analog processing unit to maintain minimal hardware resources. The core circuit that decodes the 2-D time-stamp information into optic flow was allocated in a digital chip-level processing unit. This mixed-signal circuit approach can address the drawbacks in pure analog signal processing and accurately estimate optic flows with high noise immunity with low power consumption. The estimated 16-b raw optic flow data can be further compressed to reduce the data bandwidth, also contributing the low-power operation of the sensor. The embedded 12 matched filters perform the WFI of the measured optic flows upon request, providing the compact processed information to the navigation controller. For data transfer to the host navigation controller, the sensor adopts a simple 4-wired 3MB/s serial peripheral interface (SPI). This enables modularity and expandability when multiple sensors are assembled in a hemispherical platform. Thanks to low power operation, up to 25 of the fabricated sensors can be accommodated to form a wide FoV artificial compound eye with a single 0.5g Li-battery (CP042345 from PowerStream^{TM}) for more than an hour operation.

This paper is organized as follows. In Section II, the proposed 2-D time-stamp-based optic flow algorithm is introduced. Section III describes the sensor architecture and the detailed circuit implementation of each circuit block including optic flow sensing circuits and peripheral circuits for lossless data compression and data transfer. Section IV summarizes the measured performance of the fabricated sensor. Conclusions are presented in Section V.

II. Bio-Inspired Time-Stamp-Based 2-D Optic Flow Sensing Algorithm

In order to efficiently implement the bio-inspired time-of-travel estimation, we have invented a new scheme based on time-stamp imaging. The time-stamp information is defined as the time when the most recent event (a moving feature arrival onto a pixel) occurs. The proposed scheme is illustrated in Fig. 2. In this example, the object moves with the speed of 0.5 pixel/frame for the first half of the trajectory (left arm of U), and it speeds up twice (1 pixel/frame) for the remaining movement (the right arm of U), as shown in Fig. 2 (a). As a result, the 2-D time-stamp information records the arrival time of the object in each pixel as depicted in Fig. 2 (b). Once the time-stamp information is updated, the 2-D optic flow is decoded from the information in all the pixels. The direction of motion is estimated by finding the direction of increasing time-stamp information in the neighboring pixels. The speed of the flow is inversely proportional to the time-of-travel in the given direction. Fig. 2 (c) shows the recovered 2-D optic flows based on the time-stamps.

In addition, we mimic the moving feature detection scheme of insects' visual signal pathway. The insect' eyes utilize the

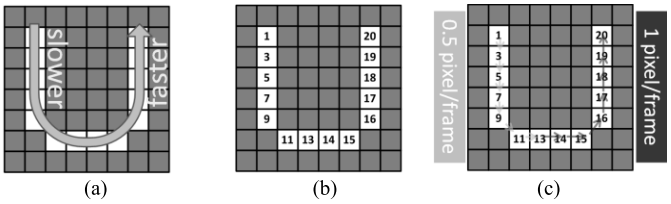

Fig. 2. Conceptual diagram of 2-D time-stamp information: (a) a trajectory of a moving object from $t = 1$ to 20, (b) time-stamp information at $t = 20$, and (c) recovered 2-D optic flow based on the time-stamps.

temporal contrast edge as an object's arrival or departure in each photo-reception unit, called an ommatidium, as illustrated in Fig. 3. Two simplified cases in the Fig. 3 are: (a) a brighter object than the background arrives at time $t = 1$ and leaves the location at $t = 2$; (b) a darker object than the background arrives at $t = 1$ and leaves at $t = 2$. A temporal high pass filter (HPF) measures the temporal contrast change. The positive polarity of the measured contrast change is named on-edge polarity. Likewise, the negative temporal contrast change is named off-edge polarity [33]. This on-edge (or also off-edge) occurs when a moving object arrives or departs in the given pixel. The on-edge (off-edge) is generated by the arrival (departure) of an object relatively brighter than the background (Fig. 3 (a)). On the contrary, the off-edge (on-edge) is generated when the relatively darker object arrives (departs) (Fig. 3 (b)). Regardless of the polarity of edges (i.e., no matter what on- or off-edge represents either arrival or departure), we can measure the time-of-travel of an object in a pixel by considering only one polarity. Fig. 3 (c) depicts that only on-edge polarity can be used to measure the traveling time of a moving object that passes neighboring two pixels. The arrival time difference between the two pixels for the same bright moving object corresponds to the time of travel of the object (Fig. 3 (d)). In the actual insects visual system, the on-edge and off-edge polarities are processed in parallel in two different cells [34]. However, our algorithm processes only one polarity to save hardware resources. This algorithm reduction is possible because the edges exist in pair and the on-edge (off-edge) of the contrast change always traces the off-edge (on-edge) contrast change if an object is passing on the pixel as shown in Fig. 3 (a) and (b).

In the proposed algorithm, we used a discrete-time high-pass filter (DT-HPF) implemented by using analog/digital (A/D) mixed-signal circuits to perform the function given by:

$$HPF_t(n) = I_t(n) - I_{t-1}(n) \tag{1}$$

where $I_t(n)$ and $I_{t-1}(n)$ are the measured illuminances at current time t and previous time $t-1$ in the spatial location of n, respectively. The algorithm only requires 1-b digital feature information at the A/D boundary defined by:

$$Feature(n) = \begin{cases} 1, & if\ HPF(n) \geq Th_{feature} \\ 0, & if\ HPF(n) < Th_{feature} \end{cases} \tag{2}$$

where $Th_{feature}$ (feature threshold) is a threshold that is an adjustable reference value to determine the moving feature. Fig. 4 summaries the implemented time-stamp-based 2-D optic flow algorithm. The moving feature detection in pixel-level

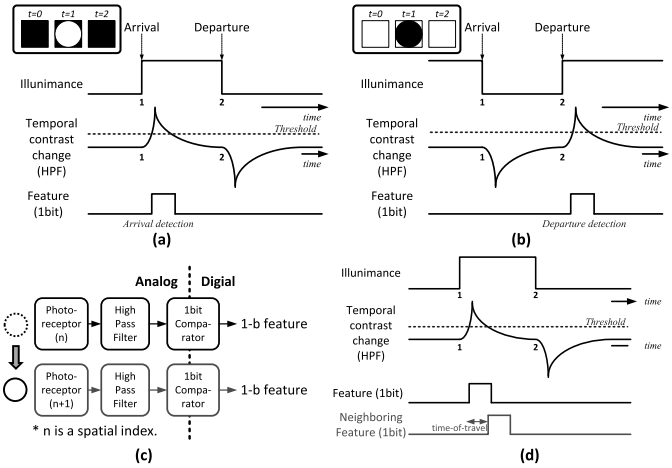

Fig. 3. A bio-inspired moving object arrival/departure detection: (a) arrival detection for a bright object, (b) departure detection for a dark object, (c) parallel moving arrival/departure detection, and (d) time-of-flight measurement.

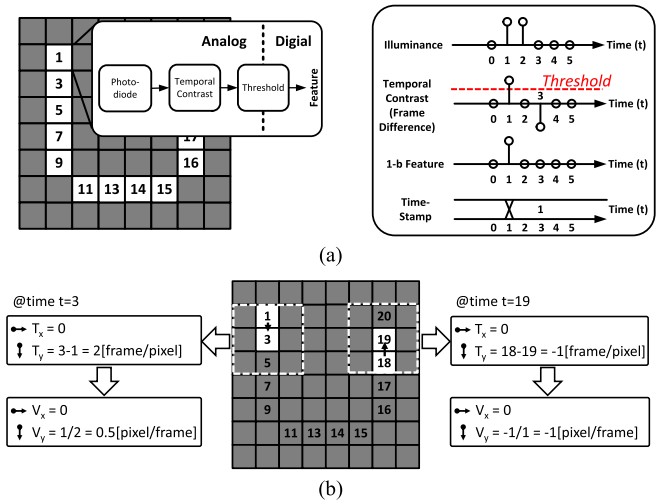

Fig. 4. Time-stamp-based 2-D optic flow estimation: (a) a moving feature detection algorithm and (b) a simplified 3×3 masking operation for optic flow measurement.

(Fig. 4 (a)) consists of a photodiode, a DT-HPF for temporal contrast measurement, and a thresholding comparator. The signals in the timing diagram represent the sampled signal at each sampling timing. In the timing diagram, on-edge contrast change is quantized using an adjustable threshold; as a result, 1-b moving feature information is detected. This feature information updates the time-stamp information of the pixel by latching the global frame counter. The time-of-travel measurement and velocity conversion can be achieved by using the updated 2-D time-stamp information as shown in Fig. 4 (b). The algorithm generates the 2-D optic flows in every pixel by referring 8 neighboring time-stamp information, which is conducted by 3×3 masking operation. For example, at time $t = 3$, the calculation is performed only at the pixel in the left dotted box. The estimation is sequentially performed by measuring the time-of-travel values in x and y directions: (T_x and T_y, respectively). This measurement is simply realized by subtracting the time-stamps of neighboring pixels from that in the center. The optic flow (V_x, V_y) which is inversely

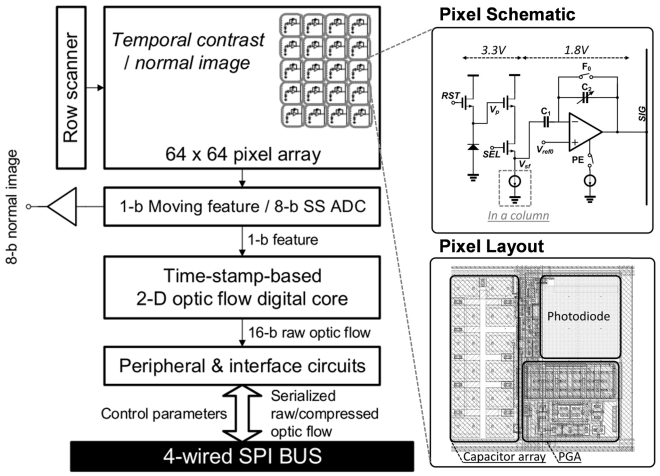

Fig. 5. Prototype time-stamp-based 2-D optic flow sensor and pixel architecture.

proportional to the measured T_x and T_y, is then generated by using look up tables.

III. Circuit Architecture and Implementation

The prototype sensor consists of three processing units: pixel-level, column-level, and chip-level signal processing units, as shown in Fig. 5. In a 64 × 64 pixel array, each pixel circuit contains a DT-HPF for the temporal contrast measurement. The column circuits realize the moving feature arrival/departure detection in each column. The chip-level circuits include the digital time-stamp-based 2-D optic flow computation core and the digital peripheral circuits to provide modular expandability for integrating multiple sensors in a module platform. To monitor temporal contrast changes, the comparator in a single-slope (SS) ADC is used for thresholding. The threshold value ($Th_{feature}$) is adjustable. The 1-b moving feature arrival or departure signal is generated if the measured positive temporal contrast (on-edge) is bigger than $Th_{feature}$. This circuit is in the boundary between the analog and digital domains, and only 1-b quantization is required for A/D conversion. This feature detection circuit is implemented column-parallel with 0.9 V supply for low power consumption.

After 1-b conversion in the column circuit, the rest of implementation will be in digital domain. The 1-b moving feature signal is fed into the digital 2-D time-stamp-based optic flow estimation core in the raster scan order. In the digital core, the delivered 1-b feature updates the 8-b time-stamp information of the corresponding pixel if a moving feature is detected. The updated time-stamp information is aligned for 3 × 3 masking operation in the two-line buffer which stores upper two rows of updated time-stamp information. Then, the core calculates four directional time-of-travel with respect to horizontal, vertical, and two diagonal axes by using the updated 3 × 3 time-stamp information. The measured time-of-travel values in four directions are converted to velocities from four look-up tables. Finally, the four converted velocities are projected to x and y axes to find 16-b 2-D optic flows: (V_x, V_y). Peripheral circuits further process the 16-b raw optic flow values. We implemented data compression algorithm to reduce the bandwidth of signal transmission. Also, the peripheral circuit is able to customize the spatial resolution of 2-D optic flows by down-sampling optic flows data in 64×64 to 32×32, 16×16, and 8×8 on demand. In addition, the on-chip WFI modulator is integrated.

A. Pixel Design

The pixel architecture and layout of the prototype sensor are shown in Fig. 5. We adopted the conventional frame-based pixel structure for two modes of operation: normal image mode and optic flow mode. In the optic flow estimation mode, each pixel measures the frame difference. The pixel includes a sampling capacitor (C_1) and a gain capacitor (C_2) to set the gain of a programmable gain amplifier (PGA). The PGA supports ×1, ×2, ×4, and ×8 gains by connecting more unit capacitors to C_2 in parallel. The supply voltage for photodiodes and source followers is 3.3 V to offer a high dynamic range. The PGA operates at 1.8 V. This will reduce static power consumption during the signal transferring period. The signal lines vertically pass through the center between the photodiode and capacitor array, and horizontally pass at the top and bottom of the pixel to achieve a higher fill factor. In this way, a pixel pitch of 28.8 μm and a fill factor of 18.3 % are achieved.

B. Column Parallel Feature Detection Circuits

Fig. 6 shows the moving feature detection circuits which are implemented in column parallel. The schematic of the full feature detection signal path is shown in Fig. 6 (a). The boundary between the in-pixel PGA and the remaining column-level circuits is divided by S_2 switch. The implemented circuits compare the measured frame difference to an adjustable feature threshold voltage ($V_{\mathrm{Th\_feature}}$); then, generate the 1-b feature information if the measured value is higher than the threshold. We deployed only off-edges of the temporal contrast to reduce the digital hardware resource with a smaller voltage headroom compared to the case that supports both edges. In Fig. 6 (b), the timing diagram illustrates the feature detection operation, which is composed of three phases: sample, hold, and compare. The timing diagram starts from the sample phase of the source follower voltage level ($V_{\mathrm{sf}}(n-1)$) by closing all F_0, F_1, and F_2 switches. At this phase, the SEL, PE, and S_1, S_2 switches are also turned on in order for V_{sf} to be stored in C_1. In the next hold phase, C_1 in each pixel holds the sampled value during the integration time by disconnecting S_2 from the column circuit and connecting S_0 to V_{ref0}, so that another rows can utilize the column detector circuits. After one frame of integration time is passed (the next sample, $V_{\mathrm{sf}}(t_n)$, is updated in each pixel), the operation moves to the compare phase. After the integration time, $V_{\mathrm{sf}}(t_n)$ is sampled in C_1 on top of the previous sample voltage: $V_{\mathrm{sf}}(t_{n-1})$. Thus the frame difference, $V_{\mathrm{sf}}(t_n) - V_{\mathrm{sf}}(t_{n-1})$, is amplified through the combination of C_1 and C_2 (Recall that F_0 is open and the PGA is enabled by setting PE as high) and is applied to V_x through the S_1 and S_2 switches, as shown in Fig. 6 (b). The measured frame difference (V_{sig}) is given by:

$$V_{sig} = -A(V_{sf}(t_n) - V_{sf}(t_{n-1})) \tag{3}$$

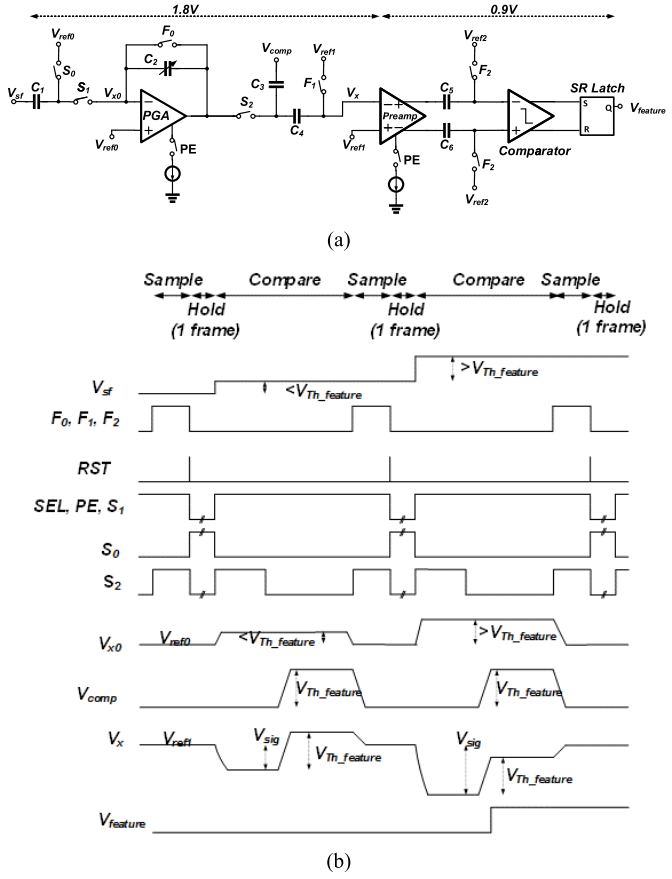

Fig. 6. Feature detection circuits: schematic and timing diagram: (a) feature detection circuit and (b) timing diagram for feature detection.

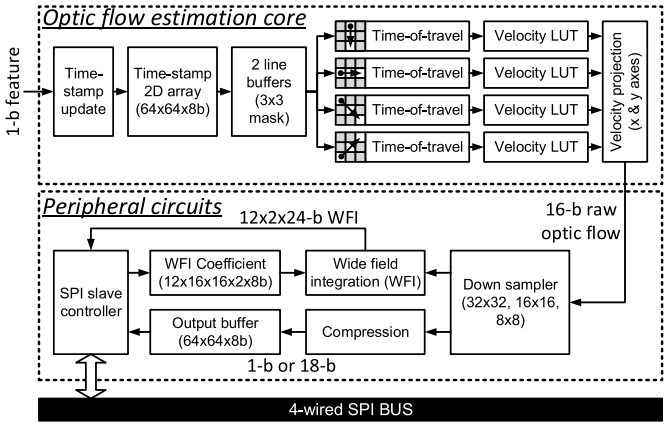

Fig. 7. Digital time-stamp-based optic flow estimation core and peripheral circuits.

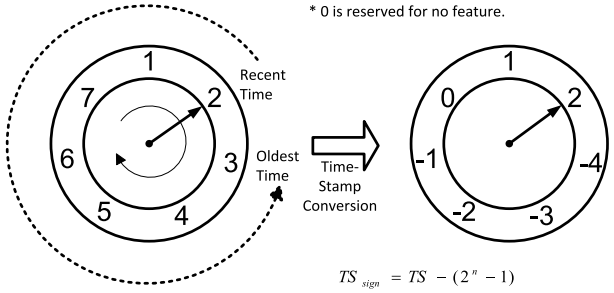

Fig. 8. Implemented circular time-stamp counter and value reordering.

where A is the gain of the PGA, which is set by the ratio of C_1 to C_2. Then, the signal path from PGA is isolated by opening S_2. The comparison (with respect to $V_{\text{Th\_freature}}$) is performed by applying the threshold voltage to the V_{comp} terminal.

C. Digital Time-Stamp Based Optic Flow Estimation Core

The block diagram of the implemented chip-level digital circuits is shown in Fig. 7. The embedded digital processing circuits mainly consist of two parts: the time-stamp-based optic flow estimation core and the peripheral circuits including SPI interface and post processors, which reduce data bandwidth (down-sampler and compressor) as well as extract WFI control parameters for MAV autonomous navigation.

The time-stamp-based optic flow core manages the 2-D time-stamp array. The first block of the diagram, which is the time-stamp update block, updates the 2-D array in each frame using the 1-b feature information from the column-level feature detector circuits. In addition, the block chronologically re-orders the time-stamp information. The implemented re-alignment algorithm is exemplified in Fig. 8. The example uses a 3-b counter. Before considering the reordering algorithm, note that zero is reserved as a time-stamp value for none moving features in the corresponding pixels. Therefore, the lowest circulating counter value is 1, and the maximum value is $2^{\text{n}} - 1$. As shown in Fig. 8, the circular counter increases clockwise. The current counter value is indicated by a solid arrow as a clock needle; thus, the current time-stamp counter is 2 in this example. This implies that the most recent event is the counter value of 2, and the oldest is 3. A dotted line illustrates the chronological relationship. To automatically recover this order, the algorithm subtracts $2^{\text{n}} - 1$ (7 for this example) only for the time-stamp values that are bigger than the current time-stamp counter (>2). As a result, the chronological order is automatically recovered by expressing the older events (than the current time stamp counter) in negative values, as shown in Fig. 8. Two-line buffers align the updated time-stamp information for 3×3 masking operation. The 3×3 time-stamp information is required to measure the velocity of a moving feature in four directions. In addition, four 1-D time-stamp-based optic flow estimation units are implemented to find 1-D optic flows for each direction using the equations in Table I. Then, velocity projection block merges the four 1-D optic flow values to generate 2-D optic flow information by projecting the measured flows onto x and y axes by using equation (4):

$$u = V_{WE} + (V_{SW\_NE} + V_{NW\_SE})/W_d$$
$$v = V_{SN} + (V_{SW\_NE} - V_{NW\_SE})/W_d \quad (4)$$

where (u, v) is the x and y directional 2-D optic flow components. V_{WE}, V_{SN}, $V_{\text{SW\_NE}}$, and $V_{\text{NW\_SE}}$ are the estimated velocities for horizontal, vertical, and two diagonal directions. W_{d} is an adjustable weight factor for the diagonal flows onto the perpendicular axes, where $\sqrt{2}$ is used in this work. The

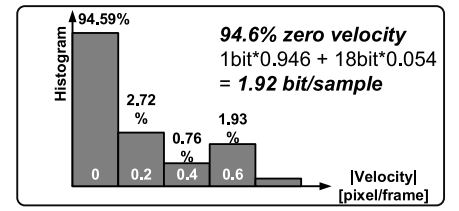

(a)

```
If (|u|<=Threshold) & (|v|<=Threshold)
{
    Send 1-b '1' code; % non-flow
}
else
{
    Send 2-b header ('01') + 16-b raw optic flow;
}
```

(b)

Fig. 9. 2-D optic flow data compression algorithm: (a) optic flow magnitude histogram in one frame and (b) compression algorithm pseudo code.

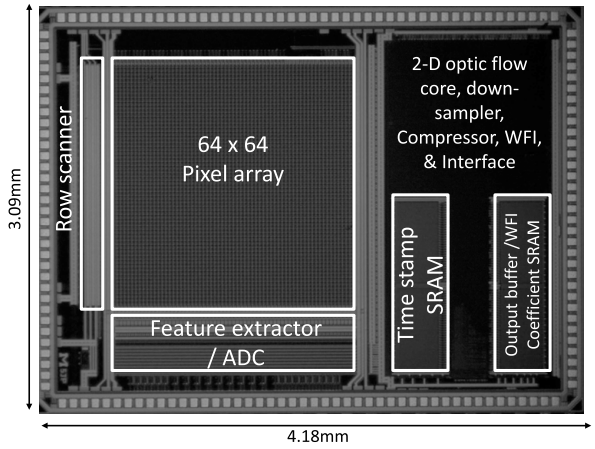

Fig. 10. Chip micrograph of the fabricated 2-D optic flow sensor.

measured u and v are 8-b each. Thus, total 16-b raw 2D optic flow data is generated from the core.

D. Optic Flow Data Compression Core

The lossless compression algorithm is depicted in Fig. 9, which is similar with the entropy encoder used in [35], [36]. The algorithm utilizes the sparsity of generated optic flows in a scene because scenes are in nature mostly composed of low spatial and temporal frequency components. We simulated using image sets from a robot simulator to verify the sparsity is consistent with the moving robot's vision [37]. The result in Fig. 9 (a) shows that only about 5.4 % of total pixels generate optic flows and the rest is static. This distribution of the histogram inspired us to apply entropy data compression technique. For simpler hardware implementation, we categorized the estimated optic flow data into only two types of data set: non-flow data and valid optic flow data. Based on the probability distribution, 16-b/sample raw optic flows can be effectively compressed to 1.92-b/sample (12.25%) in average without any loss. We introduced a threshold to determine the non-flow data for preventing negligible small flows from being degraded after compression. The sources of small flows can be a continuous weak vibration of MAVs for balancing their body. As shown in Fig. 9 (b), the criteria of determining non-flow should be applied to the condition that the absolute optic flow in both x and y directions must be less than the threshold.

E. WFI and Down-Sampler

The prototype sensor was embedded with on-chip digital WFI function. The WFI preforms the 2-D matched filtering to extract the clues of self-motion information. The 2-D matched filter measures the correlation between the optic flows and the predetermined coefficient sets and models this behavior. The filter operation is an inner product between the surrounding 2-D optic flows and user-defined 2-D coefficients [38]. The integrated WFI supports up to 12 matched filter coefficient sets that are configured through the SPI. To reduce the memory space to store the coefficients, the embedded spatial down-sampler was employed to customize a spatial resolution down to 32×32, 16×16, and 8×8. Then, the 8-b coefficients can be configured either 16×16 or 8×8 for both x and y optic flow components. Total $12 \times 16 \times 16 \times 2 \times 8$-b memory space is required. We shared the memory space with the frame buffer SRAM. Thus, in the WFI mode, the SRAM works as a coefficients set memory, while in the optic flow mode, the SRAM is used for a frame buffer to provide the data in accordance with requests from the host.

IV. Experimental Results

A prototype chip was fabricated using 0.18 μm 1P4M CMOS process and has been fully characterized. A chip micrograph is shown in Fig. 10. The total chip size is 3.09×4.18 mm^2 including I/O pads. The chip contains a 64×64 pixel array, column-level feature extraction circuits, 8-b single-slope ADCs for the normal image mode. Two SRAMs are integrated for the 2-D time-stamp array and output frame buffer/WFI coefficients storage. For the optic flow estimation, a 16 mm, f/1.7 Xenoplan lens from Schneider-Kreuznach was used.

A. 2D Optic Flow Performance

The linearity test was performed by applying a horizontally moving bar pattern on the sensor. The measured linearity curve in Fig. 11 (a) shows the results from both pure digital core and entire signal chain. The dotted triangle line with an error bar is characterized by the pure digital core. The linearity performance of the pure digital optic flow core was characterized by directly applying the digital patterns through the test ports. The triangle and error bar in the plot are the mean and standard deviation of the measured optic flow. The result shows the measured optic flow linearly follows the input velocity. The circles show the measured data from the whole sensor signal path. The mismatch between these two results may come from the imperfection of optics and/or non-uniformity in input patterns projected from LCD monitors (300 cd/m^3). We also tested a simple computer-generated patterns: translating, diagonally moving, and rotating patterns at 30 fps as shown in Fig. 11(b). The translating and diagonal

TABLE I

EQUATIONS FOR 2-D TIME-STAMP BASED OPTIC FLOW ALGORITHM

Time to move from the center	Time of Travel	Velocity
$dT_N = TS(x, y) - TS(x, y-1)$ $dT_S = TS(x, y) - TS(x, y+1)$ $dT_W = TS(x, y) - TS(x-1, y)$ $dT_E = TS(x, y) - TS(x+1, y)$ $dT_{NE} = TS(x, y) - TS(x+1, y-1)$ $dT_{NW} = TS(x, y) - TS(x-1, y-1)$ $dT_{SE} = TS(x, y) - TS(x+1, y+1)$ $dT_{SW} = TS(x, y) - TS(x-1, y+1)$	$T_{WE} = dT_W - dT_E$ $T_{SN} = dT_S - dT_N$ $T_{SW\_NE} = dT_{SW} - dT_{NE}$ $T_{NW\_SE} = dT_{NW} - dT_{SE}$	$V_{WE} = 1 / T_{WE}$ $V_{SN} = 1 / T_{SN}$ $V_{SW\_NE} = 1 / T_{SW\_NE}$ $V_{NW\_SE} = 1 / T_{NW\_SE}$

- TS(x, y) means the updated time-stamp information at the spatial location of (x, y)
- dT means the time-stamp difference between the center to neighbors.
- N, S, W, and E mean North, South, West, and East directions.
- T means the measured time-of-travel for each 1-D axis.
- V means the converted velocity for each 1-D direction.

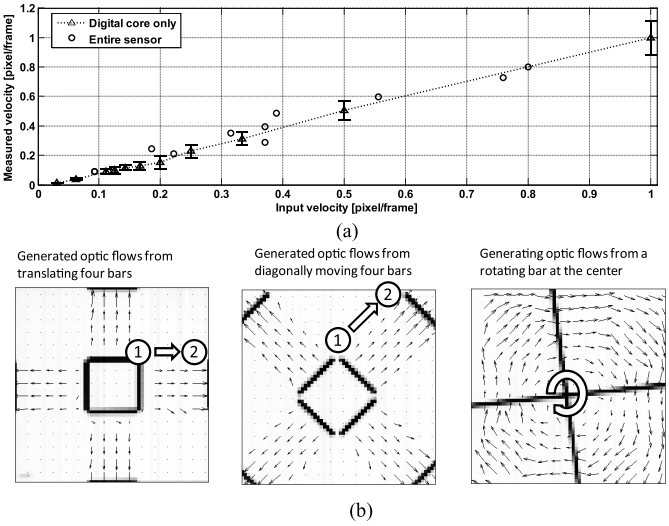

Fig. 11. Characterized 2-D Optic flow performance: (a) linearity and (b) computer generated pattern test results.

patterns were applied to verify that the four axes of time-of-travel measurement could properly operate. The bars were moving slowly for the half of the distance and speeded up for the remaining half. In addition, the accumulated 2-D optic flows from the rotating bar test pattern are also shown in Fig. 11(b).

B. Sample Images and Optic Flow From Real Objects

Sample images and captured 2-D optic flows from real moving objects are shown in Fig. 12. The image was taken in the proposed sensor operating in the normal image mode. A rotating fan, a bouncing ball and a laser pointer were used as the moving objects. The rotating fan was set up in front of the resolution chart to verify the sensor, which can capture the optic flows under the condition of complicated background patterns.

The fan was rotating with a speed of 160 rpm; the sensor captured the optic flows at a frame rate of 120 fps. The result

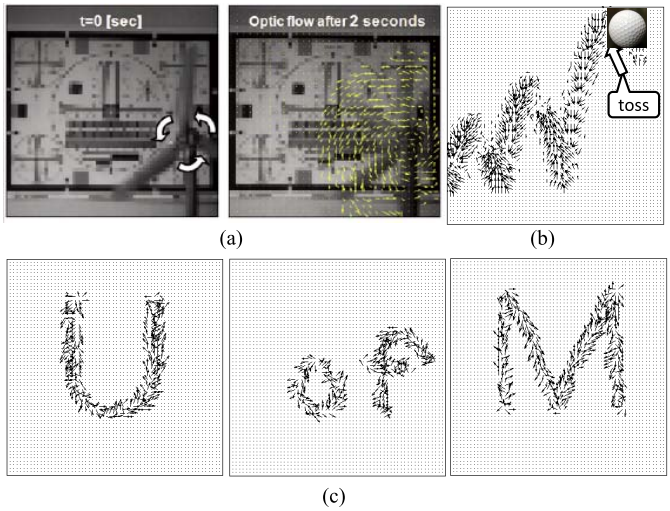

Fig. 12. 2-D optic flow tests moving objects: (a) rotating fan: 160 rpm, captured @ 120 fps, (b) bouncing ball captured @ 120 fps, and (c) letters by tracing a laser pointer source captured @ 60 fps.

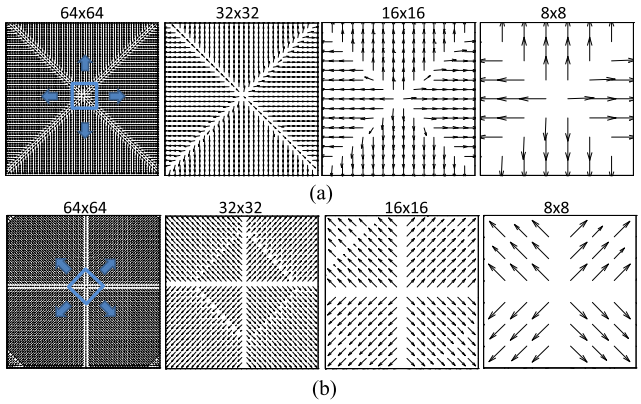

Fig. 13. Down-sampler performance. (a) Horizontally and vertically expanding square pattern and (b) diagonally expanding rhombus pattern.

TABLE II

PERFORMANCE SUMMARY FOR 2-D OPTIC FLOW SENSOR

Process	0.18 μm 1P4M CMOS		
Chip size	4.18×3.09 mm^2		
Pixel size	28.8×28.8 μm^2		
Fill factor	18.32 %		
Maximum optic flow	1.96 rad/sec @ 120 fps, FoV 60°		
[1]Power consumed in optic flow core	29.9μW	Pixel (3.3 V)	0.57μW
		Analog (0.9&1.8V)	5.30μW
		Digital (1.8V)	24.03μW
[1]Power consumed in periphery circuits	79.5μW	Digital (1.8 V)	
[1]Total power consumption	109.38 μW		
[2]Optic flow data rate (after compression)	Average: 1.92-b/sample Peak: 4.84-b/sample (< 2.8 %)		

[1]Power consumption measured @ 30 fps, [2]16-b/sample raw data

shown in Fig. 12 (a) (right) is the accumulated optic flows for 2 seconds. The trajectory of a bouncing ball was also captured by the sensor in Fig. 12 (b). Finally, a laser pointer was used

TABLE III
PERFORMANCE COMPARISON OF OPTIC FLOW SENSORS AND SYSTEMS

Reference	[3]	[5]	[9]	[15]	[17]	[18]	This work
Technology	0.35 µm CMOS	0.5 µm CMOS	N/A	N/A	0.5 µm CMOS	0.8 µm BiCMOS	0.18 µm CMOS
Processor	[1]Overo AirSTORM	N/A	BlackFin	Vertex Pro2	N/A	N/A	Custom mixed signal
Pixel Array	6 × 2 × 2	9× 1	640 × 480	N/A	17 × 17	30 × 30	64 × 64
Pixel Size [µm^2]	254 × 220 (Hexagon)	122 × 257.3	6.0 × 6.0	N/A	61 ×199	124 × 124	28.8 × 28.8
Optic Flow	1-D Digital	2-D WFI Analog	2-D Digital	2-D Digital	1-D Analog	2-D Analog	2-D Digital 2-D WFI Digital
Total Power [mW]	N/A	0.0426 @ 1kHz	184 @ 55fps	>50 @ 30fps	0.14 @ 70Hz	74.88 @ 1Hz	0.109 @ 30 Hz
FOM [nJ/pixel]	N/A	2.2	173	73	639	52	0.89/0.243 (core)

[1]Feaurting 1-GHz CPU DM3703 from Texas Instruments

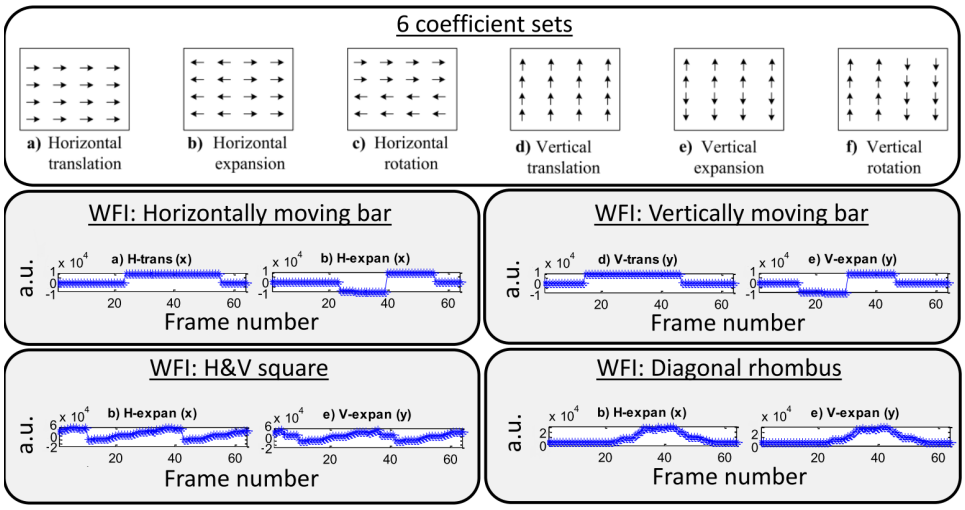

Fig. 14. WFI core performance

to test if the sensor can track the movement of a non-regular arbitrary point source movement (Fig. 12 (c)).

C. Down-Sampler and WFI

The integrated down-sampler and WFI cores were characterized by applying patterns. The generated patterns of expanding square and rhombus for the down-sampler tests are superimposed on the captured 64 × 64 flows in Fig. 13. As shown, the down-sampler finds one vector that represents 2 × 2, 4 × 4, and 8 × 8 windows for the respective down-sampling ratios. In addition, the WFI core was tested under the condition to perform 8 × 8 2-D matched filtering with 6 coefficient sets that were configured through the SPI. The coefficients are digitized into 8-b. The coefficients were set to be sensitive to 6 different self-motions as shown in Fig. 14 [12]. The plots show the WFI outputs in time. For each test, two WFI outputs from the sensitive coefficient sets of the applied motions are shown. The WFI plots successfully represent the motion of four test patterns. For example, the WFI of diagonal rhombi is symmetric to the middle of the applied period (near 40th frame) because the rhombus pattern started to break after half of the period. Then, the broken bars were shrinking for the remaining of the period.

D. Performance Summary and Comparison

The performance of the sensor is summarized in Table II. The maximum measurable optic flow is 1.96 rad/s at 120 fps. The power consumptions in the functional blocks are also decomposed at 30 fps operation. Even though the sensor requires three different power supplies (0.9, 1.8, and 3.3V) for the optimal balance between power consumption and performance, the μ-watt on-chip regulators with high power conversion efficiency (>80%) can be easily integrated [39]. To fairly compare the power consumption with other works, power figure of merit (FOM) is used [40], [41]. The FOM is defined as the power normalized to the number of pixels and a frame rate. Table III shows the FOM and the key parameters compared with the previous works. The fabricated sensor achieved the lowest power FOM to estimate 2-D optic flows mainly due to adopting the A/D mixed-signal approach. The pure digital optic flow sensing approaches require separate CPUs or FPGAs for the intensive digital computation in

addition to normal image sensors, resulting in high power consumption and a large form factor. The pure analog approaches can take advantages of reduction in bandwidth and power consumption, especially when the subthreshold circuit design technique is applied. However, these approaches suffer from large pixel circuits and unreliable operation. Thus, there is a trade-off between these two approaches for optimal power consumption and pixel scaling. Our prototype sensor achieved a power FOM of 0.89 nJ/pixel, the lowest among the reported devices up to date, by adopting the analog/digital mixed-signal approach in implementing a bio-inspired optic flow algorithm. In addition, the sensor firstly integrated the digital 2-D WFI on chip.

V. Conclusion

A bio-inspired mixed-signal 2-D optic flow sensor has been implemented for artificial compound eyes in autonomous navigation of MAVs. The sensor realized the 2-D time-stamp-based optic flow estimation core, mostly digital in the column parallel circuits, while implementing the temporal contrast feature detection in analog circuits within pixels. The optimal partition of hardware allows for efficient implementation of bio-inspired time-of-travel measurement in the mixed-signal circuits in pixel-level, column-level and chip-level blocks. The sensor also integrates peripheral circuits to provide modular expandability, which is essential to assemble multiple sensors for the artificial compound eye platform in a small form factor. The entropy data compressor reduces the full resolution 2-D raw optic flow data down to 12 % of the original data in average without any loss. More than 25 optic flow sensors can be mounted on the same platform in 3 MB/sec SPI bus. The integrated 2-D digital WFI supports up to 12 matched filters for the down-sampled 2-D optic flows (16×6 and 8×8). The sensor has successfully demonstrated to tracking optic flows for various moving objects at the maximum frame rate of 120 fps through 4 wired-SPI bus.

References

[1] S. Wu *et al.*, "Artificial compound eye: A survey of the state-of-the-art," *Artif. Intell. Rev.*, vol. 48, no. 4, pp. 573–603, 2017.

[2] Y. M. Song *et al.*, "Digital cameras with designs inspired by the arthropod eye," *Nature*, vol. 497, no. 7447, pp. 95–99, 2013.

[3] S. Viollet *et al.*, "Hardware architecture and cutting-edge assembly process of a tiny curved compound eye," *Sensors*, vol. 14, no. 11, pp. 21702–21721, 2014.

[4] R. Pericet-Camara *et al.*, "Miniature curved artificial compound eyes," *Proc. Nat. Acad. Sci. USA*, vol. 110, no. 23, pp. 9267–9272, Jun. 2013. doi: 10.1073/pnas.1219068110.

[5] A. Franceschini, J. M. Pichon, C. Blanes, and J. M. Brady, "From insect vision to robot vision," *Philos. Trans. Roy. Soc. London B, Biol. Sci.*, vol. 337, no. 1281, pp. 283–294, 1992.

[6] J.-C. Zufferey, A. Klaptocz, A. Beyeler, J.-D. Nicoud, and D. Floreano, "A 10-Gram vision-based flying robot," *Adv. Robot.*, vol. 21, no. 14, pp. 1671–1684, 2007.

[7] J.-C. Zufferey and D. Floreano, "Fly-inspired visual steering of an ultralight indoor aircraft," *IEEE Trans. Robot.*, vol. 22, no. 1, pp. 137–146, Feb. 2006.

[8] J. S. Humbert and A. M. Hyslop, "Bioinspired Visuomotor Convergence," *IEEE Trans. Robot.*, vol. 26, no. 1, pp. 121–130, Feb. 2010.

[9] J. Conroy, G. Gremillion, B. Ranganathan, and J. S. Humbert, "Implementation of wide-field integration of optic flow for autonomous quadrotor navigation," *Auton. Robots*, vol. 27, no. 3, pp. 189–198, 2009.

[10] A. M. Hyslop and J. S. Humbert, "Autonomous navigation in three-dimensional urban environments using wide-field integration of optic flow," *J. Guid. Control. Dyn.*, vol. 33, no. 1, pp. 147–159, 2010.

[11] K. Seyid, A. Richaud, R. Capoccia, and Y. Leblebici, "FPGA-based hardware implementation of real-time optical flow calculation," *IEEE Trans. Circuits Syst. Video Technol.*, vol. 28, no. 1, pp. 206–216, Jan. 2016.

[12] T. Zhang, H. Wu, A. Borst, K. Kuhnlenz, and M. Buss, "An FPGA implementation of insect-inspired motion detector for high-speed vision systems," in *Proc. IEEE Int. Conf. Robot. Autom.*, May 2008, pp. 335–340.

[13] F. Aubépart and N. Franceschini, "Bio-inspired optic flow sensors based on FPGA: Application to micro-air-vehicles," *Microprocess. Microsyst.*, vol. 31, no. 6, pp. 408–419, 2007.

[14] F. Aubépart, M. El Farji, and N. Franceschini, "FPGA implementation of elementary motion detectors for the visual guidance of micro-air-vehicles," in *Proc. IEEE Int. Symp. Ind. Electron.*, May 2004, pp. 71–76.

[15] V. Mahalingam, K. Bhattacharya, N. Ranganathan, H. Chakravarthula, R. R. Murphy, and K. S. Pratt, "A VLSI architecture and algorithm for Lucas–Kanade-based optical flow computation," *IEEE Trans. Very Large Scale Integr. (VLSI) Syst.*, vol. 18, no. 1, pp. 29–38, Jan. 2010.

[16] P. A. Shoemaker and D. C. O'Carroll, "Insect-based visual motion detection with contrast adaptation," *Proc. SPIE*, vol. 5783, p. 292, May 2005.

[17] J. Krammer and C. Koch, "Pulse-based analog VLSI velocity sensors," *IEEE Trans. Circuits Syst. II, Analog Digit. Signal Process.*, vol. 44, no. 2, pp. 86–101, Feb. 1997.

[18] F. Ruffier, S. Viollet, S. Amic, and N. Franceschini, "Bio-inspired optical flow circuits for the visual guidance of micro air vehicles," in *Proc. IEEE Int. Symp. Circuits Syst.*, May 2003, pp. III-846–III-849.

[19] S.-C. Liu, "A neuromorphic a VLSI model of global motion processing in the fly," *IEEE Trans. Circuits Syst. II. Analog Digit. Signal Process.*, vol. 47, no. 12, pp. 1458–1467, Dec. 2000.

[20] R. Moeckel and S.-C. Liu, "Motion detection circuits for a time-to-travel algorithm," in *Proc. IEEE Int. Symp. Circuits Syst.*, May 2007, pp. 3079–3082.

[21] E. Vanhoutte, S. Mafrica, F. Ruffier, R. J. Bootsma, and J. Serres, "Time-of-travel methods for measuring optical flow on board a micro flying robot," *Sensors*, vol. 17, no. 3, p. 571, 2017.

[22] R. Pericet-Camara *et al.*, "An artificial elementary eye with optic flow detection and compositional properties," *J. Roy. Soc. Interface*, vol. 12, no. 109, pp. 1–7, 2015.

[23] F. L. Roubieu, F. Expert, M. Boyron, B. J. Fuschlock, S. Viollet, and F. Ruffier, "A novel 1-Gram insect based device measuring visual motion along 5 optical directions," in *Proc. IEEE Sensors*, Oct. 2011, pp. 687–690.

[24] F. Expert, S. Viollet, and F. Ruffier, "Outdoor field performances of insect-based visual motion sensors," *J. Field Robot.*, vol. 28, no. 4, pp. 529–541, 2011.

[25] T. Delbrück and C. A. Mead, "Adaptive photoreceptor with wide dynamic range," in *Proc. IEEE Int. Symp. Circuits Syst.*, vol. 4, May/Jun. 1994, pp. 339–342.

[26] C. Posch, D. Matolin, and R. Wohlgenannt, "A QVGA 143 dB dynamic range frame-free PWM image sensor with lossless pixel-level video compression and time-domain CDS," *IEEE J. Solid-State Circuits*, vol. 46, no. 1, pp. 259–275, Jan. 2011.

[27] P. Lichtsteiner, C. Posch, and T. Delbruck, "A 128×128 120 dB 15 μs latency asynchronous temporal contrast vision sensor," *IEEE J. Solid-State Circuits*, vol. 43, no. 2, pp. 566–576, Feb. 2008.

[28] J. A. Leñero-Bardallo, T. Serrano-Gotarredona, and B. Linares-Barranco, "A 3.6 μs latency asynchronous frame-free event-driven dynamic-vision-sensor," *IEEE J. Solid-State Circuits*, vol. 46, no. 6, pp. 1443–1455, Jun. 2011.

[29] B. J. P. Hordijk, K. Y. W. Scheper, and G. C. H. E. de Croon, "Vertical landing for micro air vehicles using event-based optical flow," *J. Field Robot.*, vol. 35, no. 1, pp. 69–90, 2018.

[30] A. R. Vidal, H. Rebecq, T. Horstschaefer, and D. Scaramuzza, "Ultimate SLAM? Combining events, images, and IMU for robust visual SLAM in HDR and high-speed scenarios," *IEEE Robot. Autom. Lett.*, vol. 3, no. 2, pp. 994–1001, Apr. 2018.

[31] S. Park, J. Cho, K. Lee, and E. Yoon, "243.3 pJ/pixel bio-inspired time-stamp-based 2D optic flow sensor for artificial compound eyes," in *IEEE Int. Solid-State Circuits Conf. (ISSCC) Dig. Tech. Papers*, vol. 57, Feb. 2014, pp. 126–127.

[32] S. Park, J. Choi, J. Cho, and E. Yoon, "Bio-inspired multi-mode optic flow sensors for micro air vehicles," *Proc. SPIE*, vol. 8725, Jun. 2013, Art. no. 87251F.

[33] P. Xu, J. S. Humbert, and P. Abshire, "Analog VLSI implementation of wide-field integration methods," *J. Intell. Robot. Syst.*, vol. 64, nos. 3–4, pp. 465–487, 2011.
[34] M. Joesch, B. Schnell, S. V. Raghu, D. F. Reiff, and A. Borst, "ON and OFF pathways in *Drosophila* motion vision," *Nature*, vol. 468, no. 7321, pp. 300–304, 2010.
[35] S.-Y. Park, J. Cho, and E. Yoon, "3.37 μW/Ch modular scalable neural recording system with embedded lossless compression for dynamic power reduction," in *Proc. IEEE Symp. VLSI Circuits*, Jun. 2017, pp. 168–169.
[36] S.-Y. Park, J. Cho, K. Lee, and E. Yoon, "Dynamic power reduction in scalable neural recording interface using spatiotemporal correlation and temporal sparsity of neural signals," *IEEE J. Solid-State Circuits*, vol. 53, no. 4, pp. 1102–1114, Apr. 2018.
[37] P. A. Shoemaker, A. M. Hyslop, and J. S. Humbert, "Optic flow estimation on trajectories generated by bio-inspired closed-loop flight," *Biol. Cybern.*, vol. 104, nos. 4–5, pp. 339–350, 2011.
[38] H. G. Krapp, B. Hengstenberg, and R. Hengstenberg, "Dendritic structure and receptive-field organization of optic flow processing interneurons in the fly," *J. Neurophysiol.*, vol. 79, no. 4, pp. 1902–1917, 1998.
[39] S.-Y. Park, J. Cho, K. Lee, and E. Yoon, "PWM buck converter with $>$80% PCE in 45 μA-to-4 mA loads using analog-digital hybrid control for impiantale biomedical systems," in *IEEE Int. Solid-State Circuits Conf. (ISSCC) Dig. Tech. Papers*, Feb. 2015, pp. 218–220.
[40] J. Choi, S. Park, J. Cho, and E. Yoon, "A 1.36 μW adaptive CMOS image sensor with reconfigurable modes of operation from available energy/illumination for distributed wireless sensor network," in *IEEE Int. Solid-State Circuits Conf. (ISSCC) Dig. Tech. Papers*, vol. 55, Feb. 2006, pp. 112–113, 2012.
[41] S. U. Ay, "A 1.32 pW/frame·pixel 1.2 V CMOS energy-harvesting and imaging (EHI) APS imager," in *IEEE Int. Solid-State Circuits Conf. (ISSCC) Dig. Tech. Papers*, Feb. 2011, pp. 116–118.

Seokjun Park received the B.S. and M.S. degrees in electrical engineering from Yonsei University, Seoul, Korea, in 1998 and 2000, respectively, and the Ph.D. degree from the Department of Electrical Engineering and Computer Science, University of Michigan, Ann Arbor, MI, USA, in 2014.

From 2000 to 2008, he was a Digital Designer of camera and display processors with Samsung Semiconductor, Giheung, Korea. He continued his study on CMOS image sensors and its applications. He is currently an ASIC/IP Designer with Apple Inc., Cupertino, CA, USA. His current research interests include the hardware accelerators for artificial intelligence applications and camera processors.

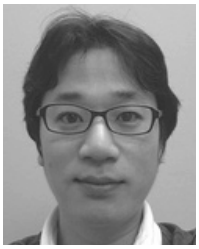

Kyuseok Lee received the B.S. degree in electrical engineering from Yonsei University, Seoul, Korea, in 2005. He is currently pursuing the Ph.D. degree with the University of Michigan, Ann Arbor, MI, USA.

From 2005 to 2012, he was with SK Hynix, where he was involved in high-speed DRAM for GPU, test structures for yield analysis, and CMOS image sensors. His current research interests are smart, low-power CMOS image sensors and neuromorphic mixed-signal processing units for a vision-based navigation system in autonomous aviation applications.

Hyunsoo Song received the B.S. and M.S. degrees in electrical engineering from Seoul National University, Seoul, Korea, in 2010 and 2012, respectively. He is currently pursuing the Ph.D. degree in electrical and computer engineering with the University of Michigan, Ann Arbor.

Until 2016, he had worked for Pixelplus Co., Ltd., Suwon, Korea, to design CMOS image sensor pixel devices. His current research interests include CMOS image sensors embedded with low latency vision processing.

Jihyun Cho received the B.S. and M.S. degrees in electrical engineering from Yonsei University, Seoul, Korea, in 2005 and 2007, respectively, and the Ph.D. degree in electrical engineering from the University of Michigan.

From 2007 to 2010, he was a Lecturer at the Korea (ROK) Air Force Academy, Cheongwon, Korea. He is currently with Apple Inc., Cupertino, CA, USA, as a System Designer. His research interests include CMOS image sensors and mixed-signal VLSI circuit design.

Sung-Yun Park received the B.S. degree in electrical engineering from Pusan National University, Busan, Korea, in 2005, the M.S. degree in electrical engineering from the Korean Advanced Institute of Science and Technology (KAIST), Daejeon, Korea, in 2008, and the M.Eng. degree in electrical and computer engineering and the Ph.D. degree in electrical engineering from the University of Michigan in 2011 and 2016, respectively.

He was involved in photonics device research with the Korean Advanced Institute of Science and Technology. From 2008 to 2010, he was a Member of the Technical Staff with Fairchild Semiconductor, Bucheon, Korea, for high voltage mixed signal circuit design. He continued his study in integrated circuits with Cornell University, Ithaca, NY, USA. From 2016 to 2018, he was a Research Fellow with the University of Michigan, where he has been an Assistant Research Scientist since 2018. In 2019, he joined the Department of Electronics Engineering, Pusan National University, where he is an Assistant Professor. His current research interests are low power, low noise mixed-signal integrated circuits and power management circuits for biomedical and sensor systems.

Euisik Yoon received the B.S. and M.S. degrees in electronics engineering from Seoul National University, Seoul, Korea, in 1982 and 1984, respectively, and the Ph.D. degree in electrical engineering from the University of Michigan, Ann Arbor, MI, USA, in 1990.

He worked with the National Semiconductor Corp., Santa Clara, CA, USA, from 1990 to 1994. He was a Member of the Technical Staff with Silicon Graphics Inc., Mountain View, CA, USA, from 1994 to 1996. He took faculty positions with the Department of Electrical Engineering, Korea Advanced Institute of Science and Technology (KAIST), Daejon, Korea, from 1996 to 2005, and the Department of Electrical and Computer Engineering, University of Minnesota, Minneapolis, MN, USA, from 2005 to 2008. During the academic year from 2000 to 2001, he was a Visiting Faculty at the Agilent Laboratory, Palo Alto, CA, USA. In 2008, he joined the Department of Electrical Engineering and Computer Science, University of Michigan, Ann Arbor, MI, USA, where he is currently a Professor and the Director of the NSF International Program for the Advancement of Neurotechnology (IPAN). He served as the Director of the Solid-State Electronics Laboratory from 2011 to 2015 and the Director of Lurie Nanofabrication Facility, University of Michigan, from 2011 to 2016.

Dr. Yoon has served on various Technical Program Committees including the Microprocesses and Nanotechnology Conference in 1998, the International Sensor Conference in 2001, the IEEE Asia-Pacific Conference on Advanced System Integrated Circuits from 2001 to 2002, the International Conference on Solid-State Sensors, Actuators, and Microsystems (transducers) in 2003 and 2005, the IEEE International Electron Device Meeting from 2006 to 2008, and the IEEE International Conference on Micro Electro Mechanical Systems in 2006 and from 2009 to 2010. He also served on the IEEE International Solid-State Circuit Conference Program Committee from 2003 to 2007 and was the General Chair of the International Symposium on Bio Micro & Nanosystems in 2005. He currently serves as an Associate Editor for the IEEE SOLID-STATE CIRCUITS LETTERS.